RESEARCH ARTICLE | FEBRUARY 14 2024

Time-resolved ion energy measurements using a retarding potential analyzer for electric propulsion applications

Austen Thomas ; Kristina Lemmer

Rev. Sci. Instrum. 95, 023505 (2024)
https://doi.org/10.1063/5.0176167

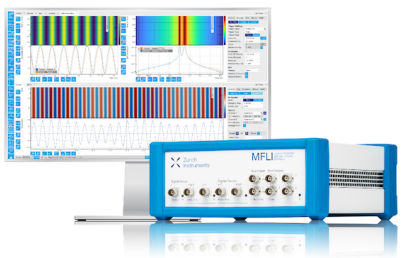

Review of Scientific Instruments ARTICLE pubs.aip.org/aip/rsi

Time-resolved ion energy measurements using a retarding potential analyzer for electric propulsion applications

Cite as: Rev. Sci. Instrum. 95, 023505 (2024); doi: 10.1063/5.0176167
Submitted: 11 September 2023 • Accepted: 21 January 2024 •
Published Online: 14 February 2024

Austen Thomas[a] and Kristina Lemmer

AFFILIATIONS

Western Michigan University, College of Engineering and Applied Science, Kalamazoo, Michigan 49009, USA

[a]Author to whom correspondence should be addressed: austen.j.thomas@wmich.edu

ABSTRACT

To completely characterize the evolving state of a plasma, diagnostic tools that enable measurements of the time-resolved behavior are required. In this study, a gridded ion source with superimposed oscillations was utilized to verify the functionality of a high-speed retarding potential analyzer (HSRPA), at frequencies equivalent to the low frequency oscillations occurring in Hall effect thrusters (HETs). The verification of this device provides an effective alternative to existing diagnostics for measuring time-resolved ion energies. Retarding potential analyzers (RPAs) have established themselves as a fundamental diagnostic in the field of electric propulsion (EP), enabling the measurement of ion energy distributions within the plumes of EP thrusters. The work presented here has demonstrated the capability of a standard RPA in conjunction with high-speed circuitry and data fusion techniques to produce time-resolved ion energy distribution functions (IEDFs) at higher frequencies and beam potentials than have previously been investigated. Tested frequencies ranged between 20 and 80 kHz with 10 V peak-to peak oscillations at a mean beam potential of 570 V. In addition, measurements were conducted with several waveforms, functioning as the superimposed oscillation, including a sine wave, triangle wave, and noisy sine wave. Data from the HSRPA were successfully reconstructed into time series utilizing two data fusion techniques: the empirical transfer function method and shadow manifold interpolation. Time-resolved IEDFs were produced at all frequency set points and waveforms. This investigation has demonstrated the HSRPA effectiveness at producing time-resolved measurements under conditions similar to those occurring in HETs.

I. INTRODUCTION

Diagnostic tools that enable measurements of the time-resolved behavior are required to fully describe the evolving state of plasma in a gas phase electric propulsion thruster. Existing high-speed diagnostic tools, such as high-speed dual Langmuir probes (HDLPs), have successfully provided insight into evolving plasma properties.[1] Recently, new methods for determining additional time-resolved plasma properties, such as ion energy, have been developed, including time-resolved laser induced fluorescence (LIF).[2] However, LIF diagnostics are costly with complex experimental setups that are difficult to move between testing facilities. A proposed alternative is the use of a standard retarding potential analyzer (RPA) with high-speed circuity to enable time-resolved measurements combined with data fusion techniques to determine the time-resolved ion energy behavior. RPAs are an electrostatic plasma diagnostic that allows the ion energy distribution function (IEDF) of the plasma to be determined. Such devices are of simple operation and construction, making them accessible and useful in experimental plasma measurements. RPAs operate by establishing a variable electric field normal to impinging ions, creating a potential barrier and filtering ions with energy less than the sourced potential. The electric field within the RPA is created with a series of electrostatically biased mesh grids. Of the grids, the retarding grid is swept over a range of potentials to screen ions based on their energy. Ions with an energy exceeding the potential barrier are able to pass the retarding grid and arrive at the collector, forming a measurable current. A relationship can be established between the collected current, I_{coll}, and the retarding grid potential, V_{bias}, forming an I–V trace. The time averaged IEDF is proportional to the negative first derivative of the I–V trace, $f(E) \approx -dI_{coll}/dV_{bias}$, and it is commonly used to approximate the IEDF. However, the exact formulation is given by

$$\frac{dI_{coll}}{dV_{bias}} = -Aqn_i\sqrt{\frac{2E}{m_i}}f(E). \quad (1)$$

Due to the simplicity of RPAs, they have found applications in numerous fields. Specifically, the use of RPAs is widespread in the field of electric propulsion (EP), where ion energy distributions are measured within the plumes of EP thrusters. Hall effect thrusters (HETs), a type of EP thruster, have significant flight heritage in commercial, military, and research-based missions.[3] Since the plasma plume of an HET is a highly dynamic environment consisting of multiple ion energy populations and exhibiting an oscillatory behavior, it is important to understand the time-resolved ion energy distribution functions in the plume, as ion energy can impact thruster performance and lifetime.[4–7] To quantify and investigate the dynamic behavior, particularly that occurs in HETs, high-speed diagnostics are required. Prior attempts to produce time-resolved ion energy measurements have been conducted with RPAs and retarding field analyzers (RFAs) by both sweeping the retarding grid and where the retarding grid potential is held constant while high-speed collector current measurements are obtained and averaged.[8–10] In prior investigations where the retarding grid was swept, the sweep rates ranged from 500 Hz as performed by Guglielmo *et al.* utilizing an RPA to 10 kHz as performed by Ochoukov *et al.* where an RFA was employed.[8,10] The fast sweeping of the RFA utilized capacitance compensation circuitry to minimize distortion due to capacitive effects. The RPA and RFA differ in the order of grid configuration; RFAs place the retarding grid directly behind the probe orifice.

Baird *et al.* developed a high-speed retarding potential analyzer (HSRPA) capable of time-resolved ion energy measurements.[11,12] This work provides a method in which a standard RPA could be used to make time-resolved ion energy measurements at frequencies and beam potentials up to 20 kHz and 150 V, respectively. The work presented in this paper utilized a gridded ion source with superimposed oscillations at higher frequencies and beam potentials to more similarly match the low frequency oscillations occurring in HETs, with a goal of verifying HSRPA functionality to measure time-resolved ion energies under these conditions. The verification of this device provides an effective alternative to existing, expensive, and complicated diagnostics for measuring time-resolved ion energies. To this end, the organization of this paper is as follows: first, an overview of the methods is provided in Sec. II, including data fusion techniques and the experimental apparatus used to perform this study. Time-resolved IEDFs for each test point are presented in Sec. III. Sections IV and V present the results obtained and a discussion of the said results, respectively. Finally, Sec. VI provides conclusions of this investigation.

II. METHODS

A known ion source with a modulated beam potential was employed to verify the capability of the HSRPA to produce time-resolved ion energy measurements. The modulated frequencies ranged between 20 and 80 kHz at a mean beam potential of 570 V, with a peak-to-peak voltage oscillation of 10 V. In addition, various waveforms were used for the modulated ion beam potential, including a sine wave, triangle wave, and noisy sine wave. The noisy sine wave was formed by superimposing a Gaussian noise with an amplitude of 10% of the original sine wave. The techniques used for the collection of data in this work follow the methods laid out by Baird *et al.*[11] Data were measured while holding the retarding grid at a constant bias and performing high-speed collector current measurements sampled at 50 MS/s. Simultaneously, a second measurement coupled to the ion source was recorded. In an HET, this will typically be the discharge current; however, for this work, the superimposed alternating current (AC) signal was measured. The process was repeated at numerous retarding grid potentials until the desired retarding bias resolution was achieved. Two low-level data fusion techniques: the empirical Transfer Function (TF) method and the Shadow Manifold Interpolation (SMI), were used to temporally reconstruct time series data forming time-resolved IEDFs.

Post-processing was accomplished by establishing a map or relationship between the system input and output, which was used for producing reconstructed waveforms and establishing time-resolved IEDFs. In this system, the collector current was used as an output, while the secondary measurement coupled to the ion source was the modulated beam potential. The chosen input signal was then mapped for each of the corresponding collector current time series measurements. The number N of respective grid potentials will result in N maps of current vs time. Each map of the collector current at a given grid potential will be used to create a set of reconstructed waveforms, which have been pseudo-triggered simultaneously, allowing a time-resolved IEDF to be obtained.[11] The two techniques used to reconstruct the time series signals are discussed in Sec. II A. It is important to note that in typical RPA experiments, corrections for the plasma potential are included; however, no such corrections were made in this work. This was deemed acceptable as the measurement technique itself is being investigated. In addition, the output of each data fusion technique has a Savitzky–Golay filter applied for smoothing noise.

A. Data fusion

Data fusion techniques enable reconstruction of temporal data from a single time series, merging the data together as if the measurements were made concurrently. These techniques allow the time-resolved response to be observed, providing insight into the evolving dynamics within a plasma discharge. The temporal reconstruction techniques used in this work are the TF method and SMI. The TF method has been used extensively in spatiotemporal reconstruction of plasma properties in HETs, demonstrating its effectiveness.[13–17] Comparatively, SMI has received less use but has shown promise in recent work.[11,18] Sections II A 1 and II A 2 detail the steps required by each method for the reconstruction of time series data. Important to a successful reconstruction of time series data using either method is the selection of various parameters discussed below. The reader is pointed to Refs. 11 and 18 for a comparison of the impact of these parameters on temporal reconstruction for both methods.

1. Empirical transfer function

The TF method utilizes the Fast Fourier Transform (FFT) algorithm to generate a transfer function relating the input and output time series. The FFT is a linear algorithm, which converts a finite dataset into frequency space revealing any periodicities, making it useful to analyze plasma dynamics. The TF method estimates system dynamics by applying the FFT to a set of simultaneously sampled input times series, $X(t)$, and output times series, $Y(t)$, from which their ratio forms the desired transfer function. In this work, $X(t)$

represents the superimposed AC signal and $Y(t)$ is the RPA collector current. There is a $Y(t)$ for each retarding grid set point, V_{bias}. The transfer function then relates the input and output signals and is used to obtain a synthetic reconstruction of the signal by multiplying the transfer function by a single sequence. A more detailed, step-by-step description of the TF method is given below.

1. Separate both input and output signals into a mean component and a time varying component. Obtaining the time-varying component is accomplished by subtracting the mean from the original signal,

$$X(t) = \bar{x} + x(\mathrm{t}), \tag{2}$$

$$Y(t) = \bar{y} + y(\mathrm{t}). \tag{3}$$

2. Apply the discrete FFT to both the input time varying component, $x(t)$, and the output time varying component, $y(t)$, to calculate the input and output complex Fourier coefficients, $A_x(k)$ and $A_y(k)$,

$$A_x(k) = \sum_{p=0}^{N-1} x(t)\exp(-2\pi ikp/N) \text{ for } k = 0 \text{ to } N-1, \tag{4}$$

$$A_y(k) = \sum_{p=0}^{N-1} y(t)\exp(-2\pi ikp/N) \text{ for } k = 0 \text{ to } N-1, \tag{5}$$

where N represents the number of Fourier coefficients and k is an index denoting the discrete frequency.

3. Compute the empirical transfer function, $H(k)$, for each V_{bias} by taking the ratio of the input to output Fourier coefficients,

$$H(k) = \frac{A_y(k)}{A_x(k)} \text{ for } k = 0 \text{ to } N-1. \tag{6}$$

4. A sequence of averaged transfer functions can be computed using

$$\overline{H(k)} = \frac{1}{Q}\sum_{q=1}^{Q}\left[\frac{\sum_{p=\frac{(q-1)N}{Q}}^{\frac{qN}{Q}-1} x(t)\exp(-2\pi ikpQ/N)}{\sum_{p=\frac{(q-1)N}{Q}}^{\frac{qN}{Q}-1} y(t)\exp(-2\pi ikpQ/N)}\right], \tag{7}$$

where Q is the number of sets averaged.

5. Apply an arbitrary known single sequence, $\overline{A_x^*(k)}$, to each transfer function establishing a set of frequency space outputs, $A_{y_{syn}}(k)$,

$$A_{y_{syn}}(k) = \overline{A_x^*(k)} * \overline{H(k)} \text{ for } k = 0 \text{ to } N-1. \tag{8}$$

6. Obtain the reconstructed, time-resolved signal, $y(t)_{syn}$, by applying the inverse Fourier transform to $A_{y_{syn}}(k)$,

$$y_{syn}(t) = \frac{Q}{N}\sum_{k=0}^{N/Q-1} A_{y_{syn}}(k)\exp(2\pi ikpQ/N) \text{ for } k = 0 \text{ to } N-1. \tag{9}$$

7. Finally, add the mean component back to the time varying component,

$$Y_{syn}(t) = \bar{y} + y_{syn}(t). \tag{10}$$

8. Plot the results of the reconstructed time-resolved signal, $Y_{syn}(t)$, for each V_{bias} over the desired time period.

The quality of the reconstruction created by the TF method is dependent on the selection of several parameters. These parameters include sample depth, sample rate, Q, and FFT window averaging. To improve the signal-to-noise ratio (SNR), large sample depths of 30×10^6 samples and a high sample rate of 50 MS/s were used in this study. In addition, the number of transfer function coefficients that were averaged was held constant at 100 and a Tukey window was chosen for FFT window averaging. This selection of parameters resulted in successful reconstructions with an SNR that approached what was observed in the SMI reconstructions. SNR is defined as the ratio of the signal power to noise power, where the signal was chosen as the RPA collector current signal at a retarding bias less than the mean beam potential and the noise signal was defined at a retarding bias over the peak ion energy, i.e., where all ion current was filtered. SNR values for the TF reconstructions ranged from 6 to 15 dB. However, SMI reconstruction ranged from 9 to 16 dB. The lowest values were obtained for the noisy sine wave, while the highest obtained were with the sine wave.

2. Shadow manifold interpolation

A different approach to temporal reconstruction is SMI, which uses a non-linear method that relies on manifold reconstruction techniques from Takens and convergent cross mapping (CCM) developed by Sugihara.[19,20] The reconstruction of temporal data can be achieved by creating shadow manifolds from time lagged samples of time series data. SMI follows a similar process to CCM, where the data are split into a training set and a test set. Each set can be used to reconstruct the other. As implemented in the TF method, $X(t)$ and $Y(t)$ represent the superimposed AC signal and RPA collector current, respectively. A description of the SMI algorithm is presented in the following, and additional information can be found in Refs. 18 and 21.

1. Split the time series $X(t)$ and $Y(t)$ into two equal halves for each V_{bias}, a training set $x(t)$ and $y(t)$ and a testing set $\tilde{x}(t)$ and $\tilde{y}(t)$, where the tilde represents a testing set. An example of this process can be seen in Fig. 1, which shows a training set (black) and a testing set (blue) for the superimposed AC signal. The RPA collector current signal shows an additional time series, the reconstructed signal (red), of which the synthesis is discussed in the following.
2. Construct a time lagged representation of embedding dimension E, by establishing E-dimensional shadow manifolds created by plotting E time lags of time series $x(t)$, resulting in the shadow manifold M_x,

$$M_{x(t)} = [x(t), x(t-\tau), \ldots \cdot, x(t-(E-1)\tau)], \tag{11}$$

where τ is the time lag of $x(t)$ in number of samples. Shadow manifolds $M_{\tilde{x}}$ and M_y are of similar form.
3. For each point in $M_{\tilde{x}(t)}$, compute the point's k nearest neighbor(s) in shadow manifold $M_{x(t)}$ using a Euclidean distance metric d_i, where k is some chosen fixed number. Both the point's nearest neighbor and the Euclidian distance can be

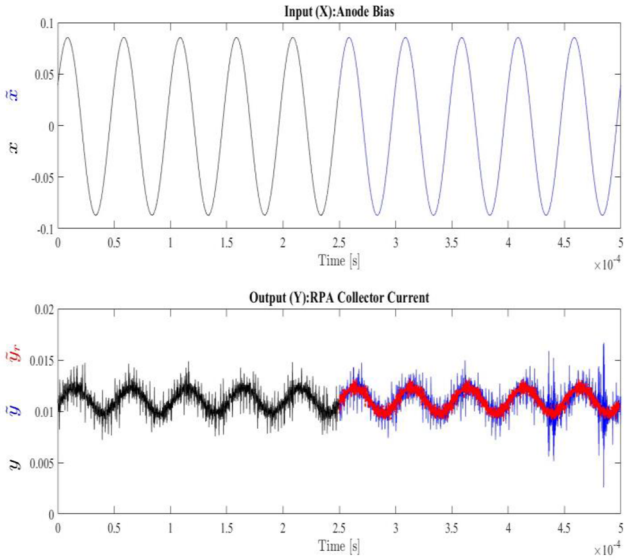

FIG. 1. SMI signal processing.

calculated through MATLAB's knnsearch() and pdist() functions, respectively. Due to M_x and M_y being causally related, the nearest neighbors in M_x and $M_{\tilde{x}}$ will also be near in M_y and the reconstructed synthetic shadow manifold $\hat{M}_{\tilde{y}(t)}$. The reconstructed synthetic shadow manifold is later determined by the linear relation shown in step 6.

4. Convert each d_i to an exponential distance,

$$u_i = \exp\left(\frac{-d_i}{\min(d_j)}\right), \tag{12}$$

where $i = (1, \ldots, k)$ and j includes all indices less than or equal to i.

5. Assign a normalized weight to each nearest neighbor,

$$w_i = \frac{u_i}{\sum_{j=1}^{k} u_j}. \tag{13}$$

6. Use w_i to estimate a reconstructed synthetic shadow manifold $\hat{M}_{\tilde{y}(t)}$,

$$\hat{M}_{\tilde{y}(t)} = \sum_{i=1}^{k} w_i M_{y(t)}. \tag{14}$$

7. Project $\hat{M}_{\tilde{y}(t)}$ back to one-dimension to obtain the reconstructed output $\tilde{y}_r(t)$, and plot the results of $\tilde{y}_r(t)$, for each V_{bias} over the desired time period, where $\tilde{y}_r(t)$ is shown in red as the reconstructed RPA collector current signal in Fig. 1.

In this investigation, the SMI parameters are held constant for uniformity among all reconstructions. Four parameters are important in the reconstruction process: the training depth, E, τ, and k. The training depth was set to 4000 samples, $E = 15$, $\tau = 1$, and $k = 50$. The selection of these parameters was based on achieving a correlation value close to unity between the measured and reconstructed outputs. The correlation value was calculated using the MATLAB's corr() function. The reconstructed time series consists of 4000 samples. A brute force strategy, discussed by Eckhardt *et al.*, was used to select τ until the desired correlation value was obtained.[18] The embedding dimension was chosen using the method laid out by Cao.[22] The selection of the time lag can have a significant impact on the outcome of the reconstruction. A small-time lag allows smaller features to be resolved but leads to a greater susceptibility to noise.[23] A value of $\tau = 1$ led to the highest correlation value in all reconstructions with an acceptable SNR. The correlation value used was the highest value obtained from a single voltage bias of an IEDF. The results of these parameter selections are shown in Sec. IV.

III. EXPERIMENTAL SETUP

This section details the diagnostic equipment, ion source, and facilities utilized in this study.

A. Retarding potential analyzer

The RPA used in this study is composed of three electrostatically biased mesh grids and a floating grid. Its construction is detailed in Ref. 12 and is illustrated in Fig. 2. The first grid encountered by ions approaching the RPA is floating to prevent the remaining grids from influencing the plasma and to attenuate any perturbations. The second and fourth grids act as electron repelling and suppression grids, respectively. These grids are biased with a set of batteries to a potential of −57 V and −36 V, respectively. The third grid is the retarding grid and is swept using a Keithley 237 source measurement unit. Finally, the collector current was measured with a FEMTO DHPCA-100 commercial transimpedance amplifier (TIA), with a bandwidth up to 200 MHz.

B. Gridded ion source

The ion source used in this study consisted of a commercial Kaufmann and Robinson 1-cm gridded ion source (KDC10) with a modulated beam supply. The KDC10 ion source traditionally uses a direct current (DC) discharge operating on argon with a standard flow rate of 4 SCCM, achieving ion beam energies ranging from 100 to 1200 eV. Laboratory power supplies were used to power all KDC10 electrodes, including the anode, which was additionally modulated to simulate low frequency oscillations. An AC signal was superimposed over the anode beam supply of the KDC10 driving the desired oscillations. This was accomplished with a Siglent SDG1032X function generator and a Solar Electronics 6220-5 audio

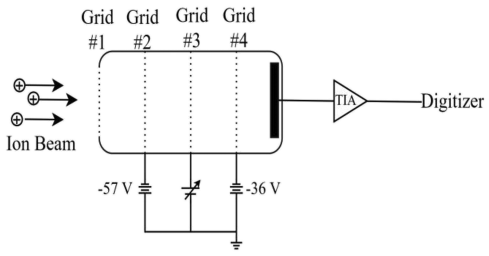

FIG. 2. Retarding potential analyzer setup.

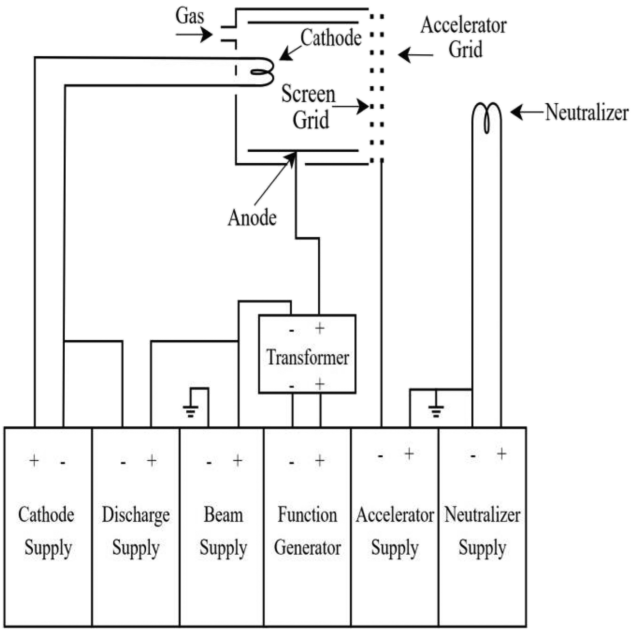

FIG. 3. Gridded ion source circuit diagram.

isolation transformer with a 2:1 step down ratio. The maximum achievable output oscillation magnitude was 10 V peak-to-peak at frequencies up to 100 kHz with a mean beam potential of 570 V. The gridded ion source setup is shown in Fig. 3.

C. Facility

All testing was conducted at Western Michigan University's Aerospace Laboratory for Plasma Experiments (ALPE) in the 1-m-diameter by 1.5-m-long Cold Plasma Experimental Research Station (CEReS) cylindrical vacuum chamber. CEReS was evacuated to high vacuum by a single cryogenic pump capable of 2000 l/s pumping capacity on air and achieving a base pressure on the order of 1×10^{-7} Torr. Operational pressures remained around 2×10^{-5} Torr throughout testing. The KDC10 was placed 295 mm upstream of the RPA, with the centerline of the RPA aligned with the centerline of the KDC10.

IV. RESULTS

The time-resolved IEDFs at each frequency are organized into Secs. IV A–IV C corresponding to the selected waveform, with each section depicting the results obtained using both data fusion techniques. The 1-cm-gridded ion source used during HSRPA testing remained at a constant beam potential of 570 V, while oscillations were superimposed over that DC beam potential with a 10 V_{pp} magnitude at frequencies of 20, 60, and 80 kHz. Throughout testing, the current collected by the RPA ranged from ~0.5 to 1.5 μA. In addition, all time-resolved IEDFs are normalized to the maximum measured value. A typical time averaged IEDF is found by differentiating the collected current to the RPA with respect to the retarding grid bias voltage. An example of a time averaged IEDF from this work is shown in Fig. 4. There are some interesting features to note in Fig. 4. First, the double peak structure is a result of the oscillatory nature of the superimposed waveforms. Second, the negative probability of the IEDF existing before 525 V occurred due to a larger collector current being measured at a greater retarding bias than the previous measurement, resulting in a negative $-dI_{coll}/dV_{bias}$. The exact cause of this negative probability is not known by the author, but it is thought be possibly due to the RPA geometry.

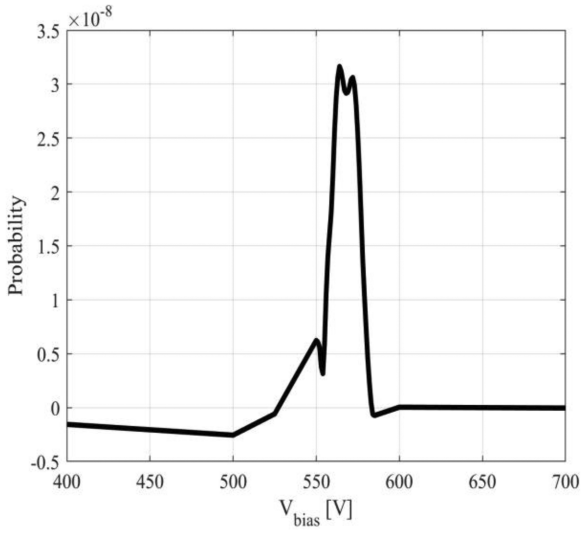

FIG. 4. Example of time averaged IEDF.

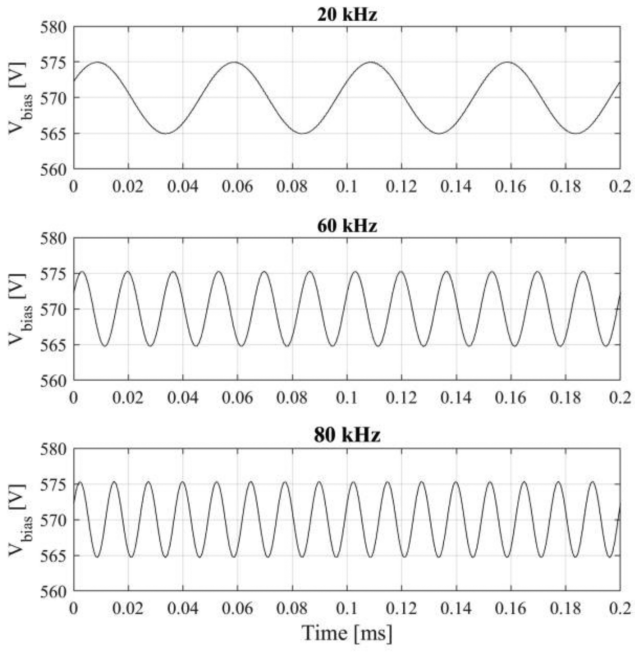

FIG. 5. Sine wave modulated beam potentials.

Existing in all time-resolved IEDFs is a time-of-flight delay of ~15 μs that results from the distance between the ion source and RPA. An additional delay results from the residence time of an ion within the RPA when there is a non-zero retarding bias on the order of 0.5 μs. However, the full-time delay is not observed in the IEDFs due to reconstruction error. This can be observed by comparing the IEDFs to the modulated anode potential for each waveform and frequency set point as seen in Figs. 5, 8, and 11. All IEDFs are normalized, where black corresponds to the minimum probability of the IEDF and white corresponds to the maximum.

A. Sine wave signals

Figure 5 shows the sine wave-imposed beam potential applied to the KDC-10 at 20, 60, and 80 kHz. Time-resolved IEDFs of the sine waveform at each frequency set point are shown in Fig. 6, reconstructed using the TF method, and in Fig. 7, reconstructed using SMI. The sine wave IEDFs show that the most probable ion energy occurs predominantly within the modulated beam potential. However, the minimum modulated beam potential is clearly exceeded by ~5 V in all reconstructions. Observed in only the 60 and 80 kHz IEDFs is an additional overshoot of the maximum beam potential. At present, the exact reasoning for these overshoots is unknown; a discussion is included in Sec. V. Another notable feature observed in all TF reconstructions, including the triangle wave, is a band of high probability that is separate from the modulated potential at a retarding bias of 556–557 V. This high probability band is attributed to a peaking in the collector current before reaching a retarding grid bias equivalent to the minimum modulated ion energy, as observed in the I–V traces. This effect is common in RPAs and can result from secondary electron emission, misalignment between the ion source and RPA, and grid imperfections.[24,25] Collectively, the TF reconstructions of IEDFs of the sine wave input were partially obscured by noise from both the experiment and the reconstruction process. In comparison, SMI is not as susceptible to noise, and thus, those reconstructed IEDFs are clearer at all frequency set points.

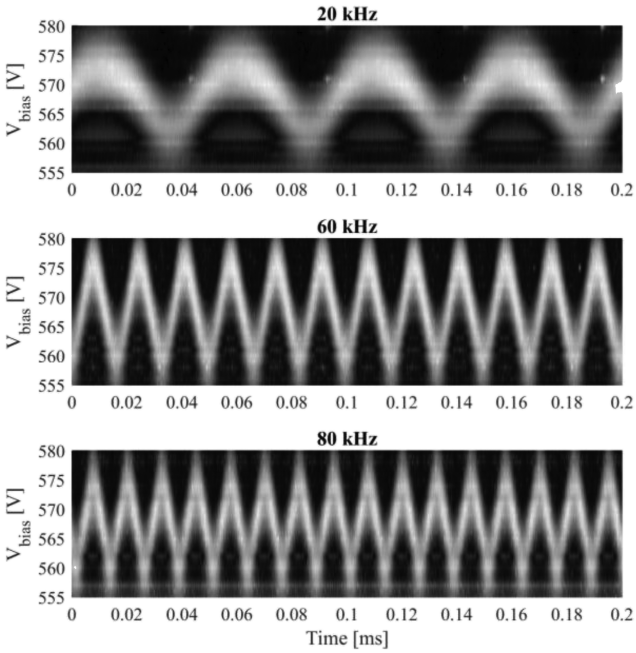

FIG. 7. Sine wave SMI reconstructions at 20, 60, and 80 kHz.

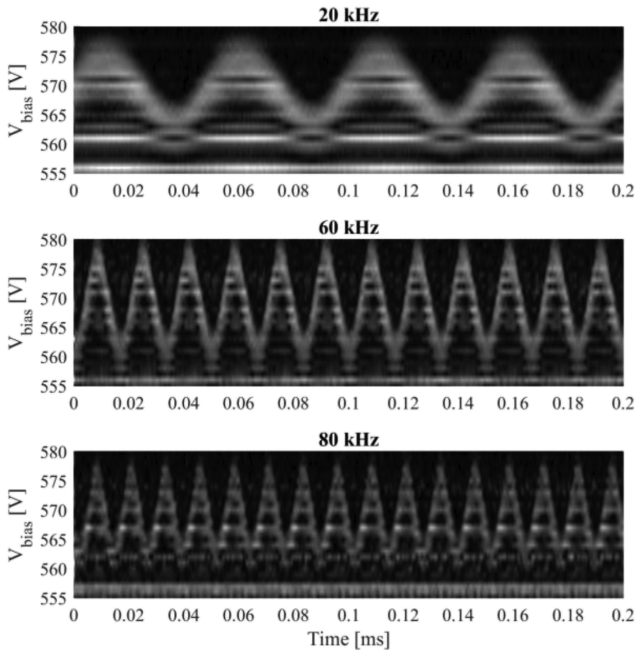

FIG. 6. Sine wave TF reconstructions at 20, 60, and 80 kHz.

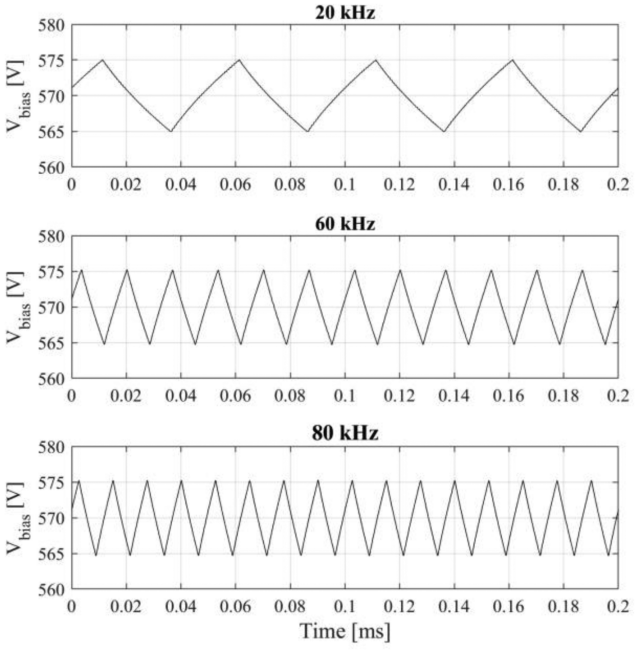

FIG. 8. Triangle wave modulated beam potentials.

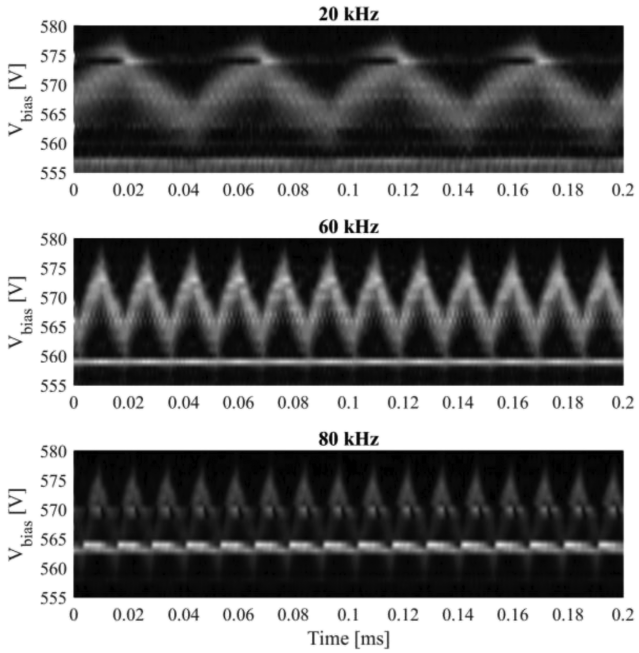

FIG. 9. Triangle wave TF reconstructions at 20, 60, and 80 kHz.

B. Triangle wave signals

Figure 8 shows the triangle wave-imposed beam potential applied to the KDC-10 at 20, 60, and 80 kHz. The time-resolved IEDFs of the triangle waveform for the TF and SMI reconstructions are presented in Figs. 9 and 10, respectively. The reconstructed triangle wave signals show IEDFs with a small overshoot, and the most probable ion energies occur well within the proximity of the modulated beam potential. The sharp points of the peaks and troughs of the IEDF are clearly distinguishable, separating the triangle wave from the sine wave. There are several notable features in the triangle wave IEDFs. First, as stated in Sec. IV A, at a retarding bias of 556–557 V, a high probability band crosses the IEDF in the TF reconstructions. In the SMI reconstructions, this band is not as obvious; rather, it appears more as a blurred region around the same retarding bias. At the 20 kHz set point, artifacts present in the IEDF are observed near the peaks in only the TF reconstructions. This may be a result of phase delay or reconstruction error. Finally, a high probability band that occurs at a retarding bias of 564–565 V resulted in less than adequate IEDFs for both data fusion techniques at the 80 kHz set point. In comparison with the other reconstructions, this high probability band is exaggerated, possibly due to beam current or experimental noise being momentarily increased. However, the primary features are still visible in the IEDF. In terms of quality, the TF and SMI reconstructions produced excellent reconstructions at 20 and 60 kHz.

C. Noisy sine wave signals

Figure 11 shows the noisy sine wave-imposed beam potential applied to the KDC-10 at 20, 60, and 80 kHz. The TF method was not capable of successfully reconstructing the noisy sine wave signals, so only the SMI reconstructions are presented. The reason for this is likely due to the fact that the TF reconstruction method is more susceptible to experimental noise.[18] Notwithstanding the SMI capability to address noise, the lack of clarity in the IEDFs is notably present in comparison with the reconstructions of previous

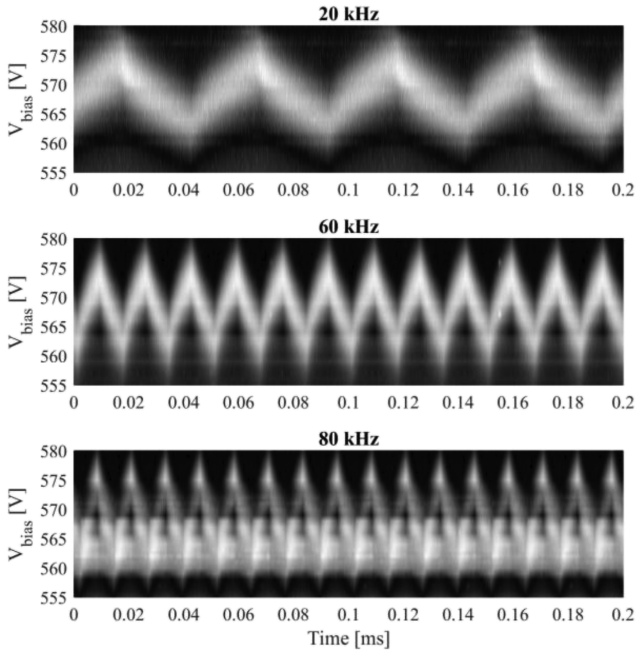

FIG. 10. Triangle wave SMI reconstructions at 20, 60, and 80 kHz.

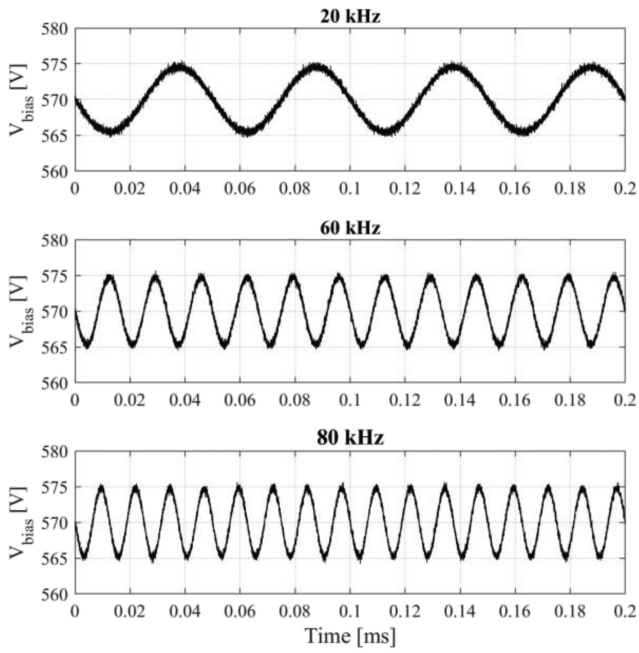

FIG. 11. Noisy sine wave modulated beam potentials.

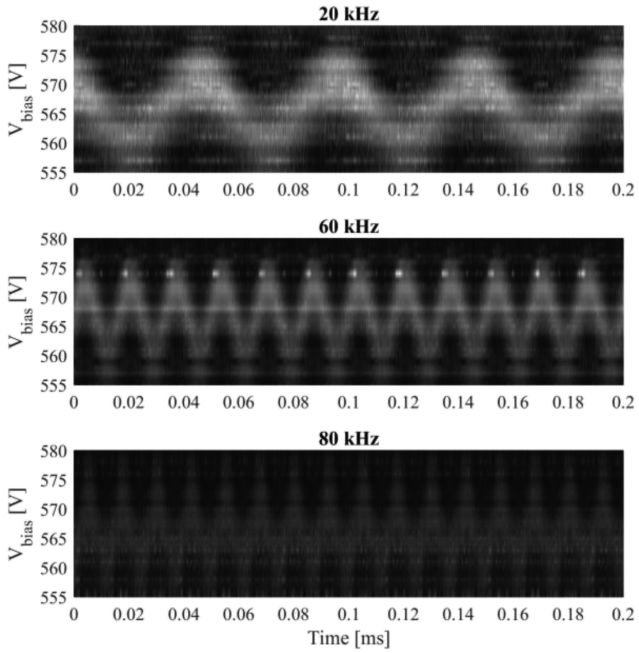

FIG. 12. Noisy sine wave SMI reconstructions at 20, 60, and 80 kHz.

waveforms. Observing Fig. 12, the IEDFs are undoubtably visible; however, they are partly blanketed in noise. The energy distribution lies within the modulated beam potential, but artifacts near the peaks and troughs of the 60 and 80 kHz IEDFs appear to obscure the full IEDF. In addition, as observed with the sine wave reconstructions, the minimum modulated beam potential was exceeded by ~5 V.

V. DISCUSSION

The time-resolved IEDFs shown in Sec. IV have been reconstructed accurately compared with the known input. Altering the type of the superimposed waveform does not have a significant effect on reconstructing the IEDFs with the exception of the 80 kHz triangle wave, where the high probability band greatly distorted the IEDF, and the noisy sine wave that could not be reconstructed with the TF method. In addition to issues regarding noise, a small overshoot and some periodic artifacts also affected the reconstruction of the time-varying IEDFs. Important to address is the 5 V overshoot of the minimum beam potential observed in the IEDFs. As stated, the exact reasoning for this overshoot is unknown. It is possible that changes in the peak-to-peak plasma potential oscillations could impact ion energy. However, as no plasma potential measurements were made, it is difficult to comment on the role of plasma potential oscillations without knowledge of its time-resolved behavior. To account for the impact of plasma potential oscillations, future experiments will include high-speed dual Langmuir probe measurements to monitor time resolved plasma potential. Also worth commenting on is the overshoot of the maximum beam potential of the 60 and 80 kHz sine wave reconstructions. The sine wave reconstructions measured the greatest magnitude of current, reaching 1.5 μA. Observing the collected current time series for the sine wave in comparison with the triangle and noisy sine waves, there exists a collected ion current beyond the expected peak ion energy, showing that more energetic ions are present in the case of the sine wave reconstructions, resulting in the increased peak ion energy. It is not known what caused this increase in peak ion energy. In addition, no potential corrections were made to account for these overshoots, as they are thought to be a real characteristic of the plasma plume behavior. Taking this offset into account with respect to the mean beam potential, an ~10% uncertainty could be claimed on ion energy measurements. As stated, future testing could include time-resolved plasma potential measurements to confirm and correlate ion energy offsets. Regardless of these challenges, the reconstructions are able to provide information on most probable ion energy as a function of time, which was the goal of the proposed research.

Both the TF method and SMI were able to effectively reconstruct the sine wave and triangle sine wave signals. However, SMI utilized only 8000 samples, while the TF method utilized 30×10^6 samples. Furthermore, even with 30×10^6 samples, the TF method was not able to discern the noisy sine wave, while SMI effectively reconstructed the noisy sine wave. In general, SMI is not as susceptible to noise due to the fact that each phase space entry in the training set corresponds to actual system states, with no requirement for periodicity and fewer constraints on smoothness. This leads to an improved performance when attempting to model nonsinusoidal characteristics in comparison with the linear nature of the TF method.[18] However, while the TF method requires larger sample depths, it is computationally more efficient, resulting in shorter times to complete a reconstruction when compared to the same sample depth. Care must be taken when comparing the computational effort required to use SMI with the sample depth and the computational and storage issues associated with the TF method. Overall, both data fusion methods show a similar signal reconstruction performance, excluding the reconstruction of the noisy sine wave signal. However, it is possible that if given a larger sample depth, the noisy sine wave signal may be able to be reconstructed using TF.

The findings of this experiment are significant as we have shown that the HSRPA can obtain time-resolved IEDFs at both a higher modulation frequency and beam potential than previously measured. We also demonstrated that the data fusion techniques are capable of reconstructing several types of waveforms. The triangle and noisy sine wave IEDFs possess features that are important to resolve, such as the distinct points in the triangle wave and the sine wave itself when enveloped in noise. These features were clearly visible in the SMI IEDFs, showing the effectiveness of the diagnostic.

As this diagnostic technique will be applied to plasma sources with more random fluctuations, it is important to comment on the ability to reconstruct time-resolved IEDFs with the random features that occur in an EP thruster. The artifacts observed in the reconstructions shown in this work are a result of the RPA geometry combined with moments of increased experimental noise. Some of these effects can be minimized or eliminated with the proper precautions, including the correct alignment of the plasma source and the RPA, correct spacing and sizing of RPA grids, the selection of a potential distribution to adequately repel and suppress electrons, and the mitigation of external noise sources. With a properly designed RPA, the HSRPA data acquisition and processing technique described should be effective at producing time-resolved IEDFs in a noisier plasma. At present, this diagnostic and

technique is capable of reconstructing signals with SNRs as defined and reported in Sec. II A. Future experiments will be conducted with an HET verifying the performance of this diagnostic in non-ideal plasma plumes.

Baird *et al.* showed the capability of the HSRPA to make measurements at lower frequencies and beam potentials using only a sine wave imposed on the beam potential of a gridded ion source.[11] The results of this work together with those of Baird have proven that the HSRPA is able to make time-resolved measurements over a wide range of frequencies and beam potentials, showing the possibility of the diagnostic to probe a range of low frequency oscillations in EP devices. Compared to methods where fast sweeping of the retarding grid is employed, the method and data fusion techniques described here are not susceptible to capacitive effects as frequency is increased. While capacitive compensation circuity can be used to prevent undesired effects, such as distorted I–V curves, higher frequencies of interest may be out of reach due to capacitive currents beginning to dominate the signal.

While this work produced satisfactory results, additional steps could be implemented to improve the quality of HSRPA measurements through both experimental and data fusion means. An experimental noise optimization study could be carried out to remove additional sources of noise and increase SNR. As an example, in this study, the TIA was placed outside of the vacuum chamber. In future studies, the TIA will be placed inside the vacuum chamber reducing the effective cable length and decreasing capacitive distortion. In terms of data fusion techniques, it would be beneficial to conduct an analysis on the optimal selection of TF and SMI parameters beyond the brute force strategy applied here.

VI. CONCLUSION

This work has demonstrated the capability of a standard RPA in conjunction with high-speed circuitry and data fusion techniques to produce time-resolved IEDFs at frequencies between 20 and 80 kHz and at an average beam potential of 570 V with three different waveforms. We were able to successfully resolve features of the waveforms measured with the HSRPA, displaying the effectiveness of this diagnostic at identifying transient features within an IEDF. Future work could include plasma potential corrections, optimization studies on experimental noise and data fusion technique parameter selection, and an increase in beam potential oscillation magnitude. The newly verified parameters of the HSRPA demonstrate that it has the ability to be utilized as a time-resolved plasma diagnostic to measure ion energy fluctuations, similar to the low frequency oscillations occurring in HETs.

ACKNOWLEDGEMENTS

This work was partially supported by NASA through the Joint Advanced Propulsion Institute, a NASA Space Technology Research Institute, Grant No. 80NSSC21K1118.

AUTHOR DECLARATIONS

Conflict of Interest

The authors have no conflicts to disclose.

Author Contributions

Austen Thomas: Data curation (lead); Formal analysis (lead); Writing – original draft (equal); Writing – review & editing (supporting). **Kristina Lemmer**: Conceptualization (lead); Funding acquisition (lead); Project administration (lead); Writing – original draft (supporting); Writing – review & editing (lead).

DATA AVAILABILITY

The data that support the findings of this study are available from the corresponding author upon reasonable request.

REFERENCES

[1] R. B. Lobbia and A. D. Gallimore, Rev. Sci. Instrum. **81**, 073503 (2010).
[2] C. J. Durot, "Development of a time-resolved laser-induced fluorescence technique for nonperiodic oscillations," Ph.D. thesis, University of Michigan, 2016.
[3] B. Yost and S. Weston, "2022 state of the art small spacecraft technology report," Report No. NASA/TP—2022–0018058, 2023, available at http://www.sti.nasa.gov.
[4] L. B. King and A. D. Gallimore, "Ion-energy diagnostics in an SPT-100 plume from thrust axis to backflow," in 34th AIAA/ASME/SAE/ASEE Joint Propulsion Conference and Exhibit, 2004.
[5] A. D. Gallimore, J. Spacecr. Rockets **38**, 441–453 (2001).
[6] J. P. Boeuf and L. Garrigues, J. Appl. Phys. **84**, 3541–3554 (1998).
[7] E. Y. Choueiri, Phys. Plasmas **8**, 1411–1426 (2001).
[8] A. Guglielmi, A. Martín Ortega, F. Gaboriau, and J. P. Boeuf, "Influence of double-stage operation on breathing oscillations and rotating spokes in the ID-HALL thruster," in 36th International Electric Propulsion Conference, 2019.
[9] T. Gibert, L. Balika, F. Diop, and A. Bouchoule, Contrib. Plasma Phys. **55**, 529–537 (2015).
[10] R. Ochoukov, M. Dreval, V. Bobkov, H. Faugel, A. Herrmann, L. Kammerloher, and P. Leitenstern, Rev. Sci. Instrum. **91**, 063506 (2020).
[11] M. Baird, R. McGee-Sinclair, K. Lemmer, and W. Huang, Rev. Sci. Instrum. **92**, 073306 (2021).
[12] M. J. Baird, T. V Kerber, K. M. Lemmer, and W. Huang, "Hall thruster plume measurements of time resolved ion energy," in 36th International Electric Propulsion Conference, 2019.
[13] R. B. Lobbia, "A time-resolved investigation of the Hall thruster breathing mode," Ph.D. thesis, University of Michigan, 2010.
[14] R. B. Lobbia and A. D. Gallimore, "Fusing spatially and temporally separated single-point turbulent plasma flow measurements into two-dimensional time-resolved visualizations," in 12th International Conference on Information Fusion, 2009.
[15] R. B. Lobbia and A. D. Gallimore, "A method of measuring transient plume properties," in 44th AIAA/ASME/SAE/ASEE Joint Propulsion Conference and Exhibit, 2008.
[16] C. J. Durot, A. D. Gallimore, and T. B. Smith, "Validation and evaluation of a novel time-resolved laser-induced fluorescence technique," Rev. Sci. Instrum. **85**, 013508 (2014).
[17] V. H. Chaplin, R. B. Lobbia, A. Lopez Ortega, I. G. Mikellides, R. R. Hofer, J. E. Polk, and A. J. Friss, Appl. Phys. Lett. **116**, 234107 (2020).
[18] D. Eckhardt, J. Koo, R. Martin, M. Holmes, and K. Hara, "Spatiotemporal data fusion and manifold reconstruction in Hall thrusters," Plasma Sources Sci. Technol. **28**, 045005 (2019).
[19] F. Takens, "Detecting strange attractors in turbulence," in *Dynamical Systems and Turbulence, Warwick 1980* (Springer, Berlin, Heidelberg, 2006), pp. 366–381.
[20] G. Sugihara, R. May, H. Ye, C.-H. Hsieh, E. Deyle, M. Fogarty, and S. Munch, "Detecting causality in complex ecosystems," Science **338**, 496–500 (2012).
[21] E. George, C. Chan, G. Dimand, R. Chakmak, C. Falcon, D. Eckhardt, and R. Martin, "Decomposing signals from dynamical systems using shadow manifold interpolation," SIAM J. Appl. Dyn. Syst. **20**, 2236–2260 (2021).

[22]L. Cao, "Practical method for determining the minimum embedding dimension of a scalar time series," Physica D **110**, 43–50 (1997).
[23]R. Martin, J. Koo, and D. Eckhardt, "Impact of embedding view on cross mapping convergence" arXiv:1903.03069 (2019).
[24]J. Ren, J. L. Polansky, and J. Wang, Plasma Sci. Technol. **16**, 1042–1049 (2014).
[25]K. M. Lemmer, A. D. Gallimore, T. B. Smith, and D. R. Austin, "Review of two retarding potential analyzers for use in high density helicon plasma," in 30th International Electric Propulsion Conference, 2007.